Article

A Sliding Mode Approach to Vector Field Path Following for a Fixed-Wing UAV

Luca Pugi [1,*], Lorenzo Franchi [2], Samuele Favilli [1] and Giuseppe Mattei [1]

1 Department of Industrial Engineering, Università degli Studi di Firenze, 50139 Firenze, Italy; samuele.favilli@unifi.it (S.F.); g.mattei@skyeyesystems.it (G.M.)
2 Sky Eye Systems SRL, 56021 Cascina, Italy; l.franchi@skyeyesystems.it
* Correspondence: luca.pugi@unifi.it

Abstract: Unmanned aerial vehicle (UAV) technology has recently experienced increasing development, leading to the creation of a wide variety of autonomous solutions. In this paper, a guidance strategy for straight and orbital paths following fixed-wing small UAVs is presented. The proposed guidance algorithm is based on a reference vector field as desired, with 16 courses for the UAV to follow. A sliding mode approach is implemented to improve the robustness and effectiveness, and the asymptotic convergence of the aircraft to the desired trajectory in the presence of constant wind disturbances is proved according to Lyapunov. The algorithm exploits the banking dynamics and generates reference signals for the inner-loop aileron control. A MATLAB&Simulink® simulation environment is used to verify the performance and robustness of the compared guidance algorithms. This high-fidelity model considers the six-degrees-of-freedom (DoF) whole-flight dynamics of the UAV and it is based on experimental flight test data to implement the aerodynamic behavior.

Keywords: UAV; waypoints; path following; lateral guidance; vector field; sliding mode; transitions

1. Introduction

In recent years, there has been an increase in interest in the study and development of unmanned aerial vehicles (UAVs) due to their suitability in many possible applications. They are being used in civil and commercial fields as well as in military operations such as intelligence, surveillance, and reconnaissance missions. In order to autonomously carry out these operations, UAVs must have path planning and tracking algorithms as well as accurate and robust guidance laws and automation onboard.

In these applications autonomously following a predefined flight route is a basic requirement for the aircraft. Path-following control causes the UAV to converge and follow a desired path with no temporal constraints.

The flight control algorithm should guarantee accuracy for the path following as well as robustness to wind disturbances [1].

Several techniques have been investigated for the path-following problem. These techniques can be divided into two categories: VTP (Virtual Target Point) techniques and control methods. The first exploits geometric approaches to generate virtual targets upon the path to be tracked in real time [2,3].

Generally, in commercial off-the-shelf autopilots, these techniques are the most popular for the path-following problem because of their simplicity and easy implementation. The control methods rely on nonlinear control theory to directly define the command signal [4–7]. Unlike the previous category where moving points are pursued, the latter

makes the cross-track error of the UAV converge to zero while maintaining a preset airspeed. To the latter category, for example, belongs the vector field (VF) technique, which involves designing a vector field to guide the aircraft on the desired path even in the presence of a constant wind disturbance [8], as well as the sliding mode control (SMC), which is a nonlinear control technique with significant robustness properties. In [9], nested saturation theory is applied to chase straight lines and orbit paths in windy conditions by developing strategies with constraints on attitude and flight path angles. More generally, SMC has been proposed for the control of airplanes since 2014 [10]. The application of SMC has found wide interest among the research community in the current year, and more generally, recently, many researchers have continued to work on this kind of approach [11–14]. Ussama et al. [11] proposed a second-order sliding mode controller of the course angle. Chen et al. [12,13] and Labbadi et al. [14] focused their attention on the rejection of lateral wind disturbances, respectively, for fixed and rotating wing UAVs.

Finally, Nian et al. [15] investigated the application of a global fast terminal sliding mode control algorithm in the path following for fixed-wing UAVs using only simulation models.

The study presented in this paper is based on the vector field notion but implements a further extension through a guidance law according to sliding mode control with the intent of improving robustness and performance. From the combination of control theory and Lyapunov stability, zero asymptotic convergence of the tracking error is ensured even in the presence of constant wind disturbances. The fixed-wing guidance problem is formulated not only for straight lines but also for orbit paths, as already addressed in the literature [12,13,16].

In this paper, the results of the proposed path-following techniques were inferred using a MATLAB&Simulink® high-fidelity model that realizes an extremely reliable simulation of the six-DoF dynamic behavior of a small fixed-wing UAV [17]. The adopted dynamic model can be divided into three parts:

- The acquisition of measurements by the sensors is simulated through the introduction of uncertainties and internal disturbances on the dynamic quantities processed by the aerodynamic block;
- The flight control system employs the guidance law to produce reference command signals for the nested PID controllers to drive motors and control surfaces of the UAV;
- High-fidelity six-DoF flight dynamics are processed by reproducing the aerodynamic behavior of the aircraft structure. The parameters of aerodynamics are derived from experimental measurements on the proposed UAV prototype and allow for the evaluation of the forces and moments acting due to flight and wind conditions.
- With respect to previously introduced works [10–16], the proposed control system is applied to a complete model of an existing VTOL developed by SkyEyeSystems. The complete dynamic model of the UAV has been previously described in a previous publication of the same authors [17] and offers some noticeable advantages with respect to previous studies such as the validated dynamics of an existing working system and the possibility of calculating the real energetic consumption exploiting a complete model of the hybrid powertrain. This is an important feature since energy consumption is a fundamental feature to evaluate how the proposed control strategy is really able to allocate available power and maximize autonomy, a fundamental requisite for AUVs.

Most path-following strategies adopt a decomposition approach to the problem: first, the path planning is carried out as well as the determination of the desired trajectory, which is used as input to the control system. This approach corresponds to the Guidance, Navigation and Control (GNC) system shown in Figure 1.
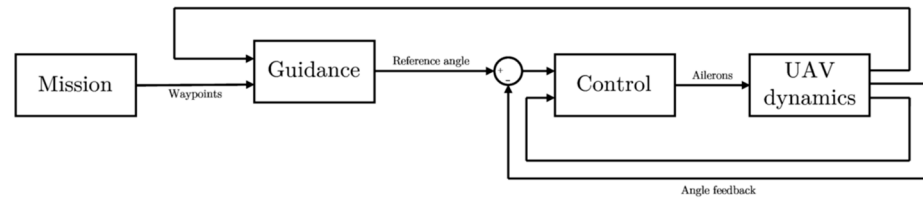
Figure 1. Guidance, Navigation and Control scheme of the proposed UAV.

All mission specifications such as desired speed and flight direction are obtained from the mission block. The route is determined by a series of time-independent target geographical locations called waypoints, whose reaching is imposed. The new target is provided to the guidance block only when the previous one is reached, according to a waypoint-switching algorithm. The logic implemented with the guidance law allows the generation of references for the control block, which exploits navigation measurements such as UAV pose and velocity to correct the flight direction and speed and compensate for the error from the planned path. Real flight conditions always involve the presence of wind, which proves to be a variable disturbance and difficult to predict. For small UAVs, the operational wind speed is commonly between 20% and 50% of the desired airspeed. Based on these considerations, an effective path-following logic must guarantee that wind-generated disturbances are tolerated by the aircraft both in the real world as well as in the simulated scenarios of this study. Wind with varying speeds was applied in the simulations to find the maximum wind tolerated by the proposed guidance laws and to obtain the corresponding indices of tracking performance to be presented.

2. Problem Statement

This chapter presents the guidance problem to be further investigated and solved. The aircraft must fly autonomously along a path that has been created through the definition of waypoints and realized as the set of segments joining two adjacent targets. Typical missions require the airspeed and altitude of the UAV to be kept constant [18].

The proposed autopilot is provided with independent controllers for velocity and altitude corrections; therefore, in this paper, the problem formulation for the fixed-wing UAV assumes that speed and altitude are held constant. The geometric problem is formalized by referring to coordinates and notable variables shown in Figure 2.
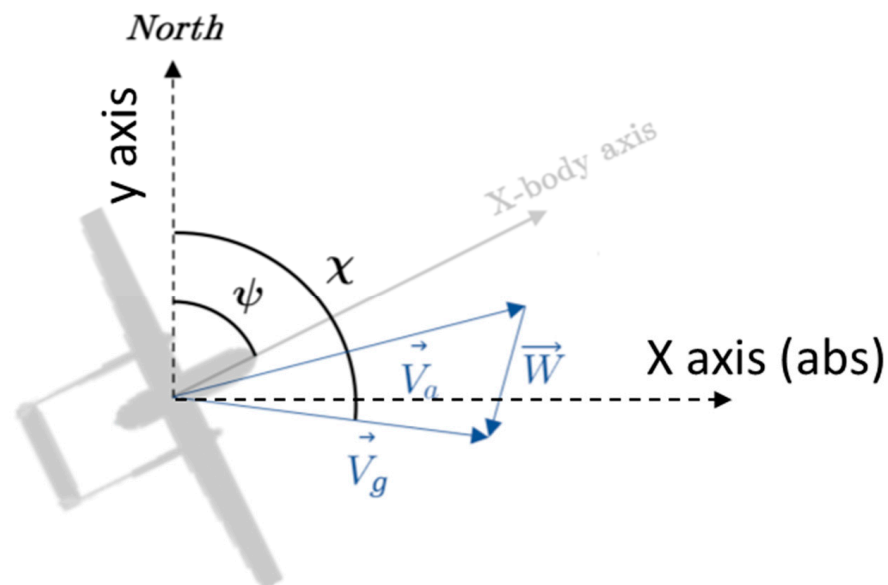
Figure 2. Definition of flight angles and speed relations.

The heading ψ and course χ angles represent the orientation of the UAV nose and ground velocity with respect to the north and they are generally controlled by guidance laws to ensure autonomous trajectory tracking. The navigation dynamic which is used to study the path-following strategy can be represented in the NED frame (with corresponding absolute axis x and y) through the definition of the ground velocity V_g (1), which differs from airspeed V_a by the vector sum of the wind velocity W (Figure 2).

$$\begin{aligned}\dot{x} &= V_a \cos\psi + W_x = V_{gx} \\ \dot{y} &= V_a \sin\psi + W_y = V_{gy}\end{aligned} \tag{1}$$

Since V_g is an inertial reference quantity, it is more convenient to express the dynamics in terms of ground speed and course angle χ rather than airspeed V_a and heading angle ψ to avoid wind dependence. Moreover, the latter are generically derived from air data instruments with eventual wind estimators, while the firsts are directly derived from GPS system measurements decreasing uncertainties.

The objective of the case study is to design a method for accurate and robust path-following in the presence of wind. The UAV must sequentially reach all waypoints with a specified tolerance while always keeping both angular and lateral tracking errors as low as possible. The guidance law must ensure proper execution of the planned trajectory along straight traits of slope ψ_w as well as upon orbit turns between them. The overall problem is thus decomposed into two subproblems for the path following:

- Straight line, where the desired path is defined as the trait joining two adjacent waypoints and where the UAV is expected to lie (Figure 3);
- Orbit path, wherein the desired path is defined as a circular orbit that can be traveled clockwise or counterclockwise at a constant distance from the center (Figure 4).
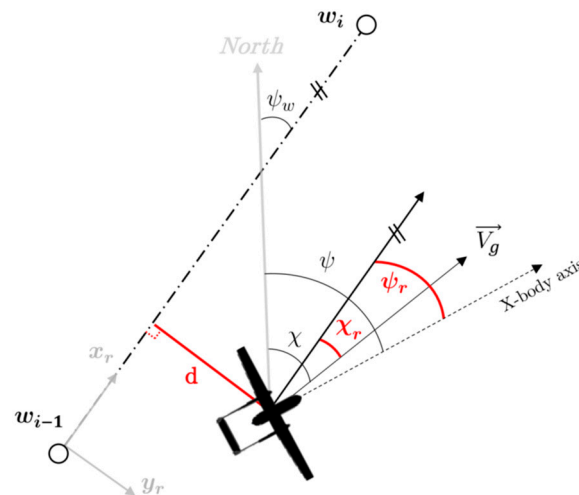

Figure 3. Straight line guidance problem.

The first consists of minimizing the cross-track error d with respect to the line $w_{i-1}\,w_i$ while simultaneously ensuring the convergence of the controlled angle $\chi- \rightarrow \psi_w$.

To simplify its treatment, the problem is formalized in a new reference frame r obtained by fixing the origin at w_{i-1} and imposing the axis x_r on the straight line.

Due to this formulation, the reference angle for control is always null and the d value is calculated from the y_r coordinate only. Figure 3 shows the quantities of interest described above and the error variables related to heading angle ψ_r and course angle χ_r, which will be used in the guidance laws along with the cross-track error.
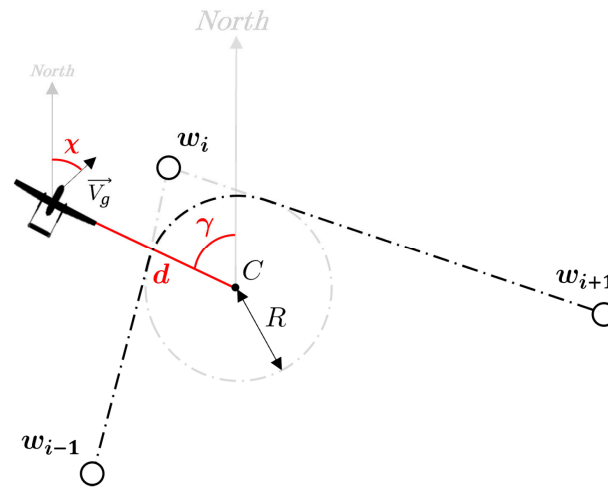
Figure 4. Orbit path guidance problem.

The circular orbit problem is treated in accordance with the straight line one and involves following an arc of a circle related to the angle between w_{i-1}, w_i and w_{i+1}. This implies that the aircraft must keep a constant distance from the center and a tangent direction to the corresponding circumference. The autopilot guarantees the convergence of the desired angle $\chi \to \gamma + \lambda \pi/2$, where λ is a binary scalar associated with the clockwise or counterclockwise direction of orbit travel, and the distance from the orbit center C is equal to the chosen radius R of curvature. In this case, the problem is evaluated in the original NED frame to avoid a moving reference during the turn. Referring to Figure 4, the gamma angle γ is defined as the angular position of the UAV with respect to the center C while d is the distance from the same center. These two variables are derived from a polar approach to the problem which results in being more suitable since the path geometry. Similarly, for the first case, the error variables used in the guidance law are derived as $\chi_r = \chi - \gamma + \lambda \pi/2$ and $d_r = d - R$.

3. Path-Following Guidance Laws

To address the previous problems, first, a vector field must be constructed. A vector field U: S $\subseteq$ Rn$-$ $\to$ Rn is a map that assigns a vector to each point of a space subset.

This method computes the vector field around the path to be followed by defining a set of desired course angles as a function of the UAV position in the XY plane. These references must point to the desired path to have convergence of the UAV toward the required route direction.

The notion of a vector field is like a potential field, which has been widely used as a tool for path planning in the robotics community, with the difference being that the first does not necessarily represent the gradient of potential but simply indicates a desired direction of flight.

The choice of a function $\sigma(d)$ for the vector field implementation is of crucial importance because it must guarantee certain properties [19]. In the case study, a scalar function that associates the desired direction χ_{des} with the cross-track error d is used (2).

$$\begin{cases} d\sigma(d) < 0 \\ \sigma(0) = 0 \\ \sigma : \mathbb{R} \to [-\chi^{\infty}, \chi^{\infty}] \end{cases} \tag{2}$$

The last condition shows how the controlled quantity is saturated to a constant value $\chi\infty$ for high values of d, while i-t changes accordingly when the cross-track error decreases.

This behavior is known as good helmsman behavior, and it is well known in the literature to better manage the trajectory [19]. The vector field method is currently applied to paths composed of straight lines and arcs. In the following subsections, this approach is applied to the creation of vector fields for the desired course angle χ_{des} to be able to keep the UAVs, respectively, along a straight path (Section 3.2 Straight line) or a circular one (Section 3.3 Orbit Path) starting from a simplified dynamics (Section 3.1 Problem Dynamics). The behavior of the proposed vector field is shown in Figure 5a,b.
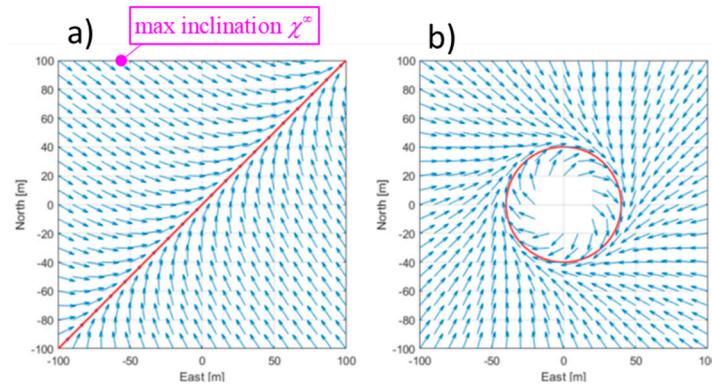
Figure 5. Calculated vector fields of χ_{des} for an example of straight path (**a**) and for an example of orbit path (**b**).

As mentioned, the objective of the paper is to obtain an effective path-following algorithm through the combination of vector field strategy with sliding mode control, which is addressed below. The term sliding mode refers to a state feedback variable structure controller that modifies the behavior of a nonlinear system by forcing it with a high-frequency control signal.

Consider the dynamics of the state variable x of a nonlinear system and define the desired state x^{des} and the corresponding error variable $\tilde{x} = x - x^{des}$ with respect to the control law defined. In the present problem, the time-variant sliding surface is defined through the scalar sliding variable s by (3):

$$s = 0 \tag{3}$$

In the scalar case under consideration, *s* turns out to be described by (4)

$$s = x^{\sim} \tag{4}$$

The goal of sliding mode control can be summarized in the following features: bring the state to the sliding surface in a finite time and keep it above. The sliding mode is based on a feedback control made of two terms:

- A model-based term built on the available model of the system, which in case of exact model knowledge, guarantees the state to remain on the sliding surface;
- A discontinuous term that forces the state on the surface in the case of drift and thus provides robustness against internal and external disturbances (e.g., model uncertainty and measurement noise).

This technique should ensure that the sliding surface is reached in a finite time and is never left; however, in reality, uncertainties in the model cause the systems not to lie exactly on the surface but within a boundary layer of limited width. The global attractiveness of

the defined sliding surface is later ensured through Lyapunov stability theory [20], indeed by choosing a positive-definite candidate function V (5).

$$V = \frac{1}{2}s^2 \tag{5}$$

Asymptotic stability is guaranteed by the condition (6):

$$\dot{V} = s\dot{s} < 0 \tag{6}$$

This condition guarantees state convergence on the sliding surface for both $s < 0$ and $s > 0$. In a real application, the intrinsic delays of the system between the sign change in s and the control action contribute to enlarging the boundary layer.

3.1. Problem Dynamics

In the present section, the overall dynamics of the notable quantities for the problem are investigated. In the field of fixed-wing aircraft, turns are performed by exploiting a component of the aerodynamic lift that allows for acceleration in the lateral direction. In aeronautics, ailerons are used to vary the lift force on the wing surface and thus produce a moment along the x-body axis; since lift is always directed along the vertical direction, such motion tilts the vector towards the inside of the curve generating the necessary centripetal acceleration. In aviation, this maneuver is referred to as banking or bank-to-turn, meaning the use of roll motion to induce the aircraft to turn [21]. This maneuver yet causes a reduction in the vertical component of the aerodynamic force, which must remain sufficient to support the aircraft's weight. For this reason, it is common in aerial applications to saturate the maximum allowable roll: in the present application, UAV roll cannot exceed $\pm\pi/6$ for flight stability reasons.

In steady state condition equations describing the banking maneuver result from balancing weight and centrifugal forces (7):

$$\begin{cases} L\cos\phi = mg \\ L\sin\phi = m\frac{V_g^2}{R} \end{cases} \tag{7}$$

where V_g is the ground speed, R is the radius of curvature and L is the lift force. The ratio of Equation (7) is known as coordinated turn approximation (8).

$$\tan\phi = \frac{V_g^2}{Rg} \tag{8}$$

In the case of stationary turn, (8) can be expressed as (9):

$$\tan\phi = \frac{V_g\dot{\chi}}{g} \tag{9}$$

From the course definition $\chi = \chi r + \psi_w$ and assuming the direction of the path invariant, (9) becomes (10):

$$if \dot{\psi} \approx 0 \Rightarrow \tan\phi = \frac{V_g\dot{\chi}_r}{g} \Rightarrow \dot{\chi} = \dot{\chi}_r = \frac{g\tan\phi}{V_g} \tag{10}$$

The other dynamics required for the guidance law design are relative to the cross-track error d, which is deduced from the geometry of the problem [10]. Since d is a variable position, its dynamics are also dependent on the ground velocity according to (11):

$$\dot{d} = V_g \sin(\chi - \overline{\chi})$$
$$\overline{\chi} = \text{course to stay on path} \tag{11}$$

3.2. Straight Line

The purpose of this study is to design a sliding mode control for the vector field strategy introduced above. In this particular section, the straight path algorithm is addressed.

In order to implement the vector field, the arctan function was chosen, since in spite of its simplicity, it allows the properties at (2) to be respected [8]: arctan is a monotonic continuous function that asymptotically saturates to a known limit value. So, by multiplying arctan for a negative constant number, it is possible to obtain a vector field function like the proposed one (12), which satisfies the following requisites such as monotonic decrease and continuity (C^∞), assuring a stable and smooth behavior of the controlled system.

The vector field for the desired angle is expressed as (12) and represented with respect to the example of a straight path in Figure 5a.

$$\chi_r^{des} = -\chi^\infty \frac{2}{\pi} \arctan(kd) \tag{12}$$

where $\chi\infty$ denotes the value of saturation for high values of d, which, in our case, was chosen to be equal to $\pi/4$, according to the good helmsman behavior. The parameter k defines the slope of the trajectory around zero instead, and thus for small lateral tracking errors. In order to avoid excessive control efforts, k cannot be chosen arbitrarily large despite being beneficial for tracking performance near the desired path. According to Equation (4), the sliding surface can be designed as (13), whose dynamic is expressed by (14).

$$s = \chi_r + \frac{1}{2}\arctan(kd) = 0 \tag{13}$$

$$\dot{s} = \dot{\chi}_r + \frac{\dot{d}}{2}\frac{k}{1 + (kd)^2} = \dot{\chi}_r + \frac{V_g}{2}\frac{k}{1 + (kd)^2}\sin\chi_r = 0 \tag{14}$$

In order to define the guidance law, it is necessary to infer the model-based and discontinuous terms. In the case of exact knowledge of the model, the continuous term would guarantee a constant s and thus the stability of the equilibrium point. Referring to Equations (10) and (11) for dynamics and imposing (14) to be zero, (15) is obtained

$$\frac{g\tan\phi}{V_g} + \frac{V_g}{2}\frac{k}{1 + (kd)^2}\sin\chi_r = 0 \tag{15}$$

The model-based term ϕ_{mb} of the command signal that verifies this condition is the following (16)

$$\phi_{mb} = \arctan\left[-\frac{V_g^2}{2g}\frac{k}{1 + (kd)^2}\sin\chi_r\right] \tag{16}$$

The discontinuous term allows the rejection of measurement and model uncertainties and ensures asymptotic convergence to the desired equilibrium point. The function chosen

for this purpose is k sign(s), which completes the command signal ϕ_{des}. The overall guidance law is finally expressed as (17):

$$\phi_{des} = \arctan\left\{ \frac{-V_g^2}{2g} \frac{k}{1+(kd)^2} \sin\chi_r - \kappa\ sign\left[\chi_r + \frac{1}{2}\arctan(kd)\right] \right\} \tag{17}$$

The general demonstration of asymptotic stability, viable for both the straight and circular paths, is deferred later.

3.3. Orbit Path

In the problem formulation, both straight lines and circular arcs were shown as feasible paths to follow. The reference vector field is designed similarly to the previous case. The geometry of the orbit is defined by a fixed center and a constant radius. The implemented algorithm must command the ground speed towards the center for high distances from the predefined path ($\chi_\infty = \pi/2$), as the distance decreases in a tangential direction to the arc. From these considerations, the desired course is chosen as (18) and represented with respect to an example of an orbit in Figure 5b.

$$\chi^{des} = \gamma - \lambda\frac{\pi}{2} - \arctan[k(d-R)] \tag{18}$$

where R is the radius of the orbit, λ generalizes the formulation with respect to the direction of rotation around the center and k is the parameter specifying the transition rate from $\gamma - \pi$ and $\gamma - \lambda\ \pi/2$. The analysis of the problem as polar formulation requires the dynamics of the corresponding variables dd/dt and $d\gamma/dt$. The latter indicates the velocity relative to the orbit and is thus defined as (19):

$$d\dot{\gamma} = V_g \cos\left(\chi - \gamma + \lambda\frac{\pi}{2}\right) \Rightarrow \dot{\gamma} = \frac{V_g}{d}\sin(\chi - \gamma) \tag{19}$$

In analogy with (11), (20) is obtained:

$$\dot{d} = V_g \cos(\chi - \gamma) \tag{20}$$

Equivalent to what was carried out for the straight path, the sliding surface and its dynamics for the specific case are derived

$$s = \chi - \gamma + \lambda\frac{\pi}{2} + \arctan[k(d-R)] \tag{21}$$

$$\dot{s} = \dot{\chi} - \dot{\gamma} + \frac{k}{1+[k(d-R)]^2}\dot{d} \tag{22}$$

Again, the continuous term is determined by imposing invariant surface dynamics on (23) and substituting Equations (10), (19) and (20).

$$\frac{g\tan\phi}{V_g} - \frac{V_g}{d}\sin(\chi - \gamma) + \frac{k}{1+[k(d-R)]^2}V_g\cos(\gamma - y) = 0 \tag{23}$$

From (23), the model-based term ϕ_{mb} is derived (24)

$$\phi_{mb} = \arctan\left\{ \frac{V_g^2}{gd}\sin(\chi - \gamma) - \frac{k}{1+\left[k(d-R)^2\right]}\frac{V_g^2}{g}\cos(\chi - \gamma) \right\} \tag{24}$$

The resulting command signal ϕ_{des} inclusive of the discontinuous term is expressed as (25)

$$\phi_{des} = \arctan\left\{ \frac{V_g^2}{gd}\sin(\chi-\gamma) - \frac{k}{1+\left[k(d-R)^2\right]}\frac{V_g^2}{g}\cos(\chi-\gamma) - \kappa sign\left[\chi-\gamma+\lambda\frac{\pi}{2}+\arctan(kd-kR)\right]\right\} \quad (25)$$

Equation (17) together with (25) allows precise following of a path realized as the combination of straight and circular sections. Regardless of the definition of surface and path geometry, a generalized demonstration of Lyapunov stability can be arranged.

As mentioned in the theory above, asymptotic stability is guaranteed by condition (6).

In both cases (straight or circular/orbit path), the control signal ϕ_{des} and the ds/dt equation can be substituted in the stationary turn condition (9), obtaining Equation (26).

Passages shown in (26) are referred to as the straight path case for which the passages are shorter; however, the sequence of passages needed to obtain (26) for the orbit path is almost the same.

$$\phi_{des} = \arctan\left\{ \frac{-V_g^2}{2g}\frac{k}{1+(kd)^2}\sin\chi_r - \kappa\,sign[\chi_r + \tfrac{1}{2}\arctan(kd)]\right\}$$

$$\Downarrow$$

$$\frac{-V_g^2}{2g}\frac{k}{1+(kd)^2}\sin\chi_r - \kappa\,sign[\chi_r + \tfrac{1}{2}\arctan(kd)]$$

$$\overbrace{\tan\phi} \qquad\qquad = \frac{V_g\dot\chi_r}{g} \qquad (26)$$

$$\Downarrow$$

$$\frac{V_g}{g}\,\overbrace{\dot{s}}^{(\dot\chi_r+V_g\frac{k}{1+(kd)^2}\sin\chi_r)} = -\kappa\,sign\,\overbrace{(s)}^{\chi_r+\frac{1}{2}\arctan(kd)} \Rightarrow \dot{s} = -\kappa\frac{g}{V_g}sign(s) = -\kappa\frac{g}{V_g}\frac{|s|}{s}$$

The stability condition (6) can be rewritten as (27), by substituting the time derivative of s with Equation (26).

$$\overbrace{\left(-\kappa\frac{g}{V_g}\frac{|s|}{s}\right)}^{\dot{s}}s = -\kappa\frac{g}{V_g}|s| < 0 \quad (27)$$

Stability condition (27) is always verified for $\kappa > 0$. This proves to be a sufficient condition for the attractivity of both the sliding surfaces; hence, the state trajectory will always be directed and remain on the desired equilibrium point regardless of the initial condition. When the state of the system is in the proximity of the surface ($s = 0$), the discontinuous term commutes at a very high frequency between $\pm\kappa$. This phenomenon, known as chattering, causes inefficiencies due to the effort induced on the control signal [22]. Among the various methodologies in the scientific literature, the most commonly adopted is the boundary layer approximation, which implements a bonded saturation instead of the sign operator, which is a bit stiff for a real numerical implementation.

4. Results

4.1. Simulation Model for Validation and Verification of Proposed Path Control Strategy

Proposed control strategies have been simulated on a full model of a fixed-wing drone that also takes count of the 3D aerodynamic approach proposed as an example by Borup [23], introducing further refinements since the UAV is decomposed in a sum of rigid aerodynamic bodies (wings, ailerons, etc., to which three-dimensional aerodynamic coefficients are applied), whose properties are described both in terms of matrices representing both aerodynamical and inertial terms [17]. The model also includes not only the lumped modeling of inertial and aerodynamic behavior but also the complete modeling of the

propulsion layout including propellers, electrical motors, ESC, and the internal combustion engine of the drone, which is supposed to have a hybrid propulsion layout which allows series–parallel hybrid management of the propulsion system. The complete model of the UAV developed in Matlab-Simulink™ has been the object of a previous publication by the same authors [17]. The model that has been used for the purpose of this paper has been validated with specific experimental tests which have been mainly focused on the identification of the efficiency of the propulsion system (propellers, motor, etc). To make comprehension easier for the reader, some data of the simulated UAV are shown in Table 1 refers to the hybrid propulsion layout represented in Figure 6: the UAV is equipped with vertical propellers to ensure VTOL (Vertical Take Off and Landing) capabilities. These vertical propellers are not of practical interest for simulation performed in this work since they are disabled when the UAV is cruising in fixed-wing mode. Two longitudinal propellers are installed; the first is directly connected to the ICE engine, assuring the base performance for cruising, while a second electrical one (series connected) is used to boost system performances. The whole system is fed by an ICE motor which also recharges an onboard storage system. Data concerning the calculation of fuel consumption, known from experimental activities, are shown in Figure 7: the motor is regulated to work on the maximum relative efficiency curve (magenta profile in Figure 7), the nominal working condition being almost coincident with the absolute maximum efficiency. The proposed model is implemented in Matlab-Simulink with a partitioning of sub-model in atomic tasks (running with fixed sampling rates), which makes the RT implementation relatively easier on different real-time targets of the whole model or alternatively of single modules like the proposed path control. In this way, model [17] can be used as a tool for HIL and SIL testing of the proposed path control algorithms. In this work, the chosen RT target is a DSPACE MicroLabBox.

**Table 1.** Main features of the Benchmark UAV model adopted for simulation of the proposed path control.

Weight [kg]	Wingspan [m]	Oper. Speed [m/s]	Thurst of Vert. Props [kgf]	Power of Vert. Props [W]	ICE Long. Prop. Thrust [kgf]	ICE Long. Prop. Power [W]	Elec. Long. Prop. Thrust [kgf]	Elec. Long. Prop. Power [W]	ICE POWER [W]	ICE Displacement [cm^3]	Total Installed Storage [Ah]
43.5	3.6	24	13.3	3200	6	1515	6.5	3744	1500	29 2 Stroke	49 (6 s)

4.2. Vector Field and Sliding Mode Control: Comparison Through Simulation Results

In this section, vector field and sliding mode control guidance laws are compared for results and to conclude the best choice in terms of the trade-off between performance robustness and cost of the algorithm. Afterward, different strategies for transitioning between consecutive straight-line paths will be investigated. The following metrics/indexes are considered:

- Norm-1 $||d||_1$ is used as an effectiveness parameter and it is mostly indicative of the magnitude of small oscillations around the planned path;
- Root mean square error RMSE (d) also allows the evaluation of the path-following performance, heavily penalizing wide deviations from the desired path;

- Fuel consumption: fuel is used as an indirect parameter of the control effort of the generic law. Fuel consumption is calculated since the proposed controller is tested on a full model of the drone which includes not only validated and detailed aerodynamics but also a complete description of the behavior of the propeller, motors and of hybrid propulsion system (ICE, batteries and energy management systems). The complete model has been described in a previous publication by the same authors [17].

(**a**)

(**b**)

(**c**)
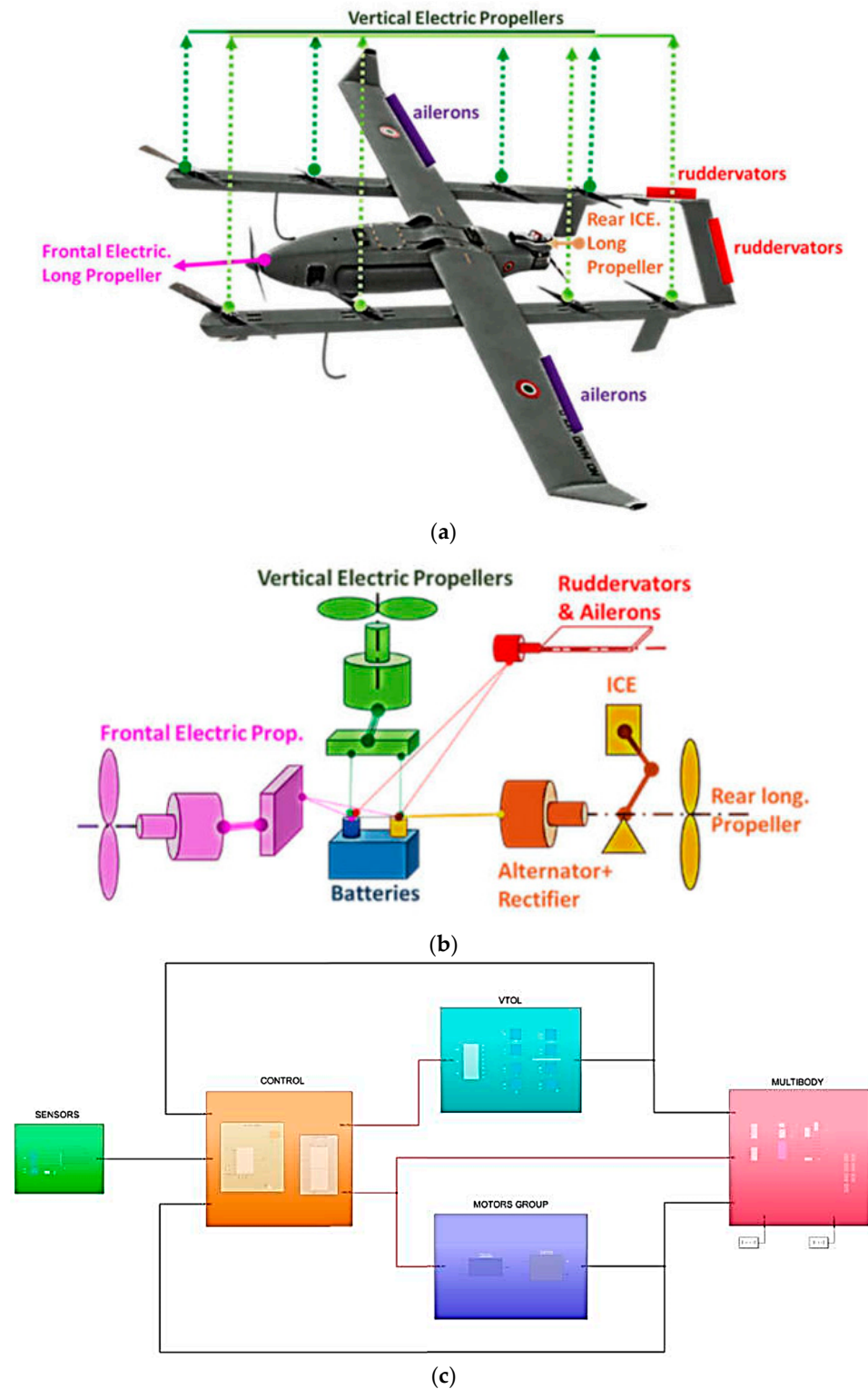
Figure 6. Propulsion (**a**), power management layout (**b**) [17] and corresponding Matlab-Simulink simulation model (**c**).
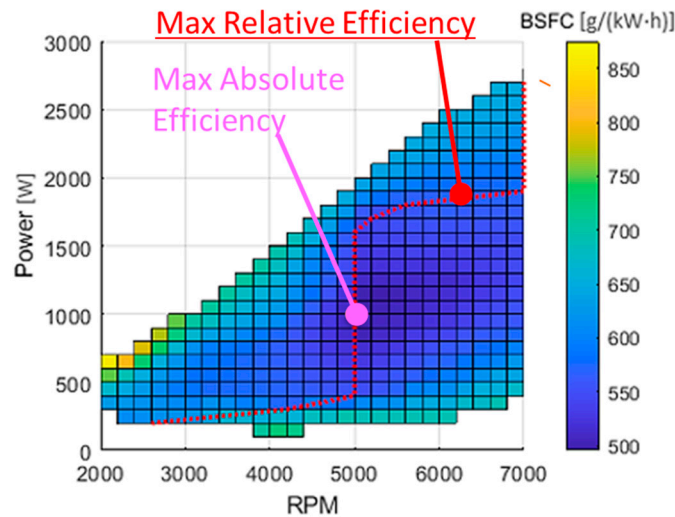
Figure 7. Efficiency of installed ICE [17].

For the reader's convenience, each of the above strategies is associated with an acronym:

VFH: vector field guidance law based on controlling the heading angle ψ though;
VFC: path-following strategy for vector field course χ;
SMC: sliding mode control algorithm applied to VFC law.

For the explanation of the results, a square route, shown in Figure 8, is chosen to be simulated because, by symmetry, fixing a north wind W, the aircraft is impacted on all sides during flight. The maximum tolerated wind will be the one for which the UAV can reach all waypoints within a range of 50 m (value equal to 9 m/s). The first comparison concerns the vector field VF only, which is applied to both the heading ψ and course χ angles in order to confirm the greater control effectiveness of the latter. The illustrated results are obtained with (Figure 8a) and without wind applied (Figure 8b). Applied wind disturbance has an amplitude of 9 m/s.
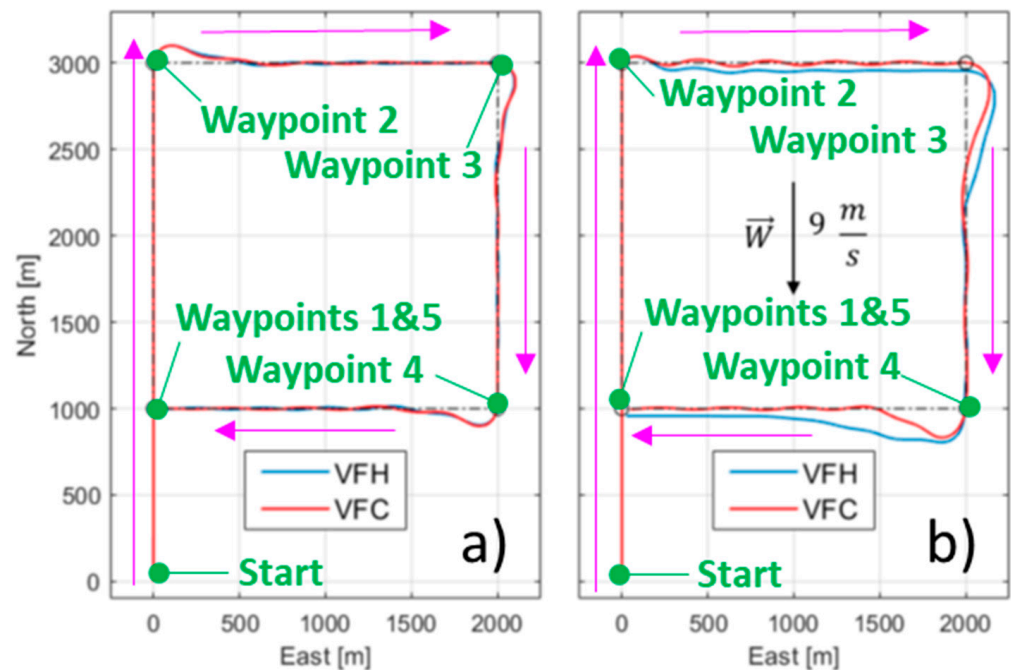

Figure 8. Comparison of vector field algorithms, (**a**) without wind disturbance, (**b**) with a fixed crosswind disturbance of 9 [m/s].

In Figure 8a, the trajectories generated by the two algorithms are really similar since, in the absence of wind, as shown in Figure 8b, the two controlled variables differ due to wind as suggested by (1); however, the adopted model [17] is able to reproduce some typical behaviors that can be reproduced only by an accurate three-dimensional model of the system:

- When turning around waypoint 2, the wind disturbance helps both controllers to implement a sharp curve for the following reasons:
  - The UAV is turning right and the crosswind is coming from the right, producing both transversal drag and an increased roll of the airplane that improves the turning capacity.
  - When traveling from waypoint 1 to 2, the wind disturbance negatively affects the absolute speed of the plane, reducing the centrifugal inertial terms during the curve around waypoint 2.
- On waypoint 3, wind disturbance increases system overshot since the wind drives the plane from the back, producing a sign inversion of the drag and a rapid acceleration that penalizes the controllability of the plane.
- On waypoint 4, the worst turning behavior is verified before approaching the curve on the waypoint the plane is accelerated by the wind from the back. As the plane turns right, the wind drives the plane from the left. In this case, increased lateral drag proposed by the wind causes an increased curving radius (an overshoot) for the same reason that lateral wind induces a reduced roll of the plane, reducing the turning capability of the plane.

The observed behavior of the model confirms the capability of the model to reproduce a near-realistic response.

In contrast, in Figure 8b, the improvement obtained with the VFC algorithm in terms of wind tolerance is evident. The reason for this improvement can be deduced from the observation of Figure 9a,b, which shows how in VFC the UAV nose tends to head to the wind direction (Figure 9b), therefore providing a more aerodynamic profile and reducing drag forces.

The test confirms that the course angle is the best to use as a controlled quantity in the guidance law as it can handle the wind more successfully. Once the heading variable is excluded, the comparison between VFC and SMC guidance laws is reported in Figure 10. The SMC law is developed by a sliding mode approach to the vector field algorithm and based on the same angle χ to accomplish better results. The test scenario is like the previous one: the maximum wind tolerated by both algorithms is found and implemented in the square path. In this case, the applied wind disturbance is much higher and corresponds to the maximum wind disturbance that can be applied with respect to the propulsion performances of the plane (19 m/s). This is clearly advisable when the UAVs fly against the wind (from waypoint 1 to waypoint 2): the oscillating upwind pace of the plane is a clear indication of the marginal power and stability margin available against additional drag forces produced by the incoming wind.

On the first side of the path (from waypoint 1 to waypoint 2), the behavior of the UAV controlled with the VFC is more nervous causing inefficiencies and thus increased consumption, while with the SMC, such behavior is mitigated because of its upper limit and its derivative term, which damps oscillations around the path. The third side (from waypoint 3 to waypoint 4) is the most critical for both techniques because of the strong influence a tailwind has on the UAV's aerodynamics. The area with the most pronounced divergence is the last curve (from waypoint 4 to waypoint 5), where the difference between

the waypoint-switching over-elongation is evident (around waypoint 4) due to the different control efforts produced by the two techniques.
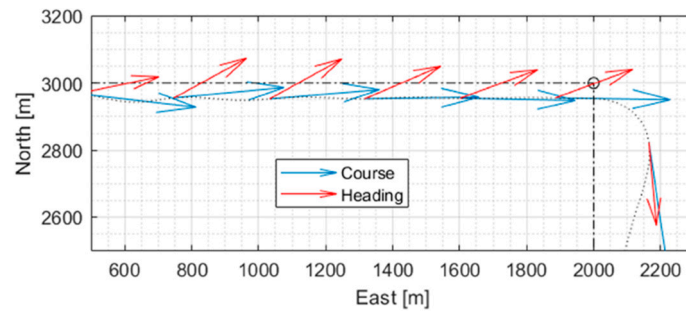
(a) Vector Field Heading (VFH)
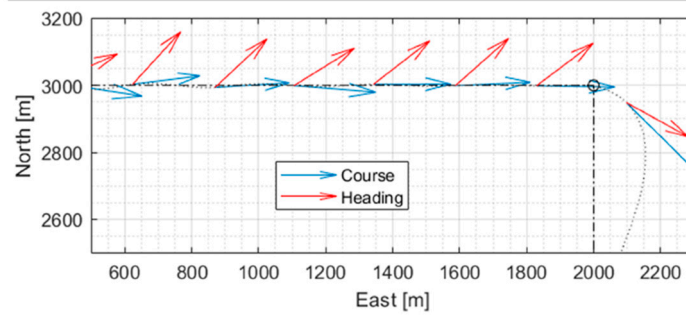
(b) Vector Field Course (VFC)

Figure 9. Comparison of heading (**a**) and course VF control (**b**) in the presence of wind disturbances.
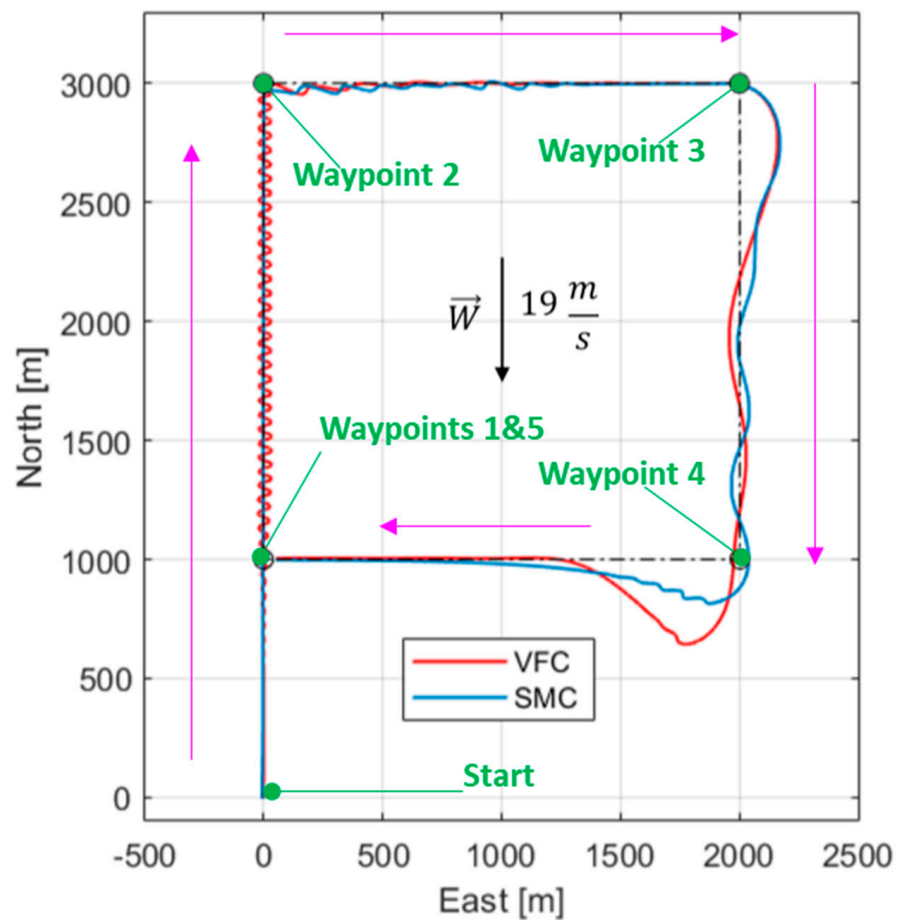

Figure 10. Comparison of course-based control algorithms in a high-wind scenario.

A comparison of the performance according to the indices proposed above is reported. Table 2 shows the results for Figure 10's scenario with a wind disturbance of 19 m/s. The same table also shows the performance of SMC with an increased wind disturbance of 22 m/s, which is not tolerated by VFC and becomes completely unstable with this higher wind disturbance.

Table 2. Performance of course-based algorithms at the maximum tolerated wind intensity.

	Wind [m/s]	$||d||_1$ [m]	RMSE(d) [m]	Fuel [g]	Mission Duration [s]
VFC	19	22.43	63.99	119.61	917.05
SMC	19	10.66	25.03	102.52	883.48
SMC	22	21.18	61.39	197.74	1731.38

Simulations prove a clear superiority of the SMC algorithm with respect to both performance and efficiency. The performance in the respective wind boundary conditions is comparable; however, an increase in power consumption and mission time is noted but mainly due to the stronger wind, which requires more thrust and causes lower ground velocities. In the final analysis, the two course-based algorithms are built and deployed on hardware to be run for a portability test.

The adopted hardware is the MicroLabBox dSPACE®, which is a high-performance dual-core platform. Its results are oversized for this purpose but also very accurate and reliable in computational capacity. Both the guidance laws are run at 400 Hz, simulating the mission scenario in Figure 8, and turnaround times and overruns are recorded. Turnaround time is the measurement of the computational time needed to complete the task with respect to the maximum time assigned by the real-time scheduler of the board.

The SMC algorithm results are 15% slower to be run with respect to the VFC one. The higher computational load is not enough to deny the SMC superiority in performance and efficiency, since for the assigned RT target, both algorithms exploit, respectively, the 20% and the 22.5% of the available resources in terms of turnaround time.

4.3. Polygonal Path Test

As shown in Figure 11a, tests with proposed path controllers have been repeated considering polygonal closed paths with an increasing number of sides. In this way, it is possible to perform turns of different angular amplitude applying the same wind disturbance in different directions. The aim of this test was to evaluate the dynamic performances of path controllers over a wider population of turns. The length of the side of each closed polygonal path is constant and equal to 2000 m. In this way, it is possible to observe the behavior of the vehicle after a turn along a straight path which is always the same length. For example, in Figure 11b, results concerning an octagonal path are shown. In this way, it was possible to calculate the maximum transversal errors associated with the turn on the i-th waypoint. These results are shown in Figure 12a–c. Also, residual oscillations after each turn at the *i*-th waypoint are described in the space domain x_{traj}, where x_{traj} is defined as the longitudinal coordinate/traveled distance along the reference path. The oscillation period is dimensionally a distance in meters so frequencies ω_i are the corresponding reciprocal. The decaying of observed oscillations in terms of transversal path errors is approximated with the free response of a second-order system with a damping ratio ξ_i.
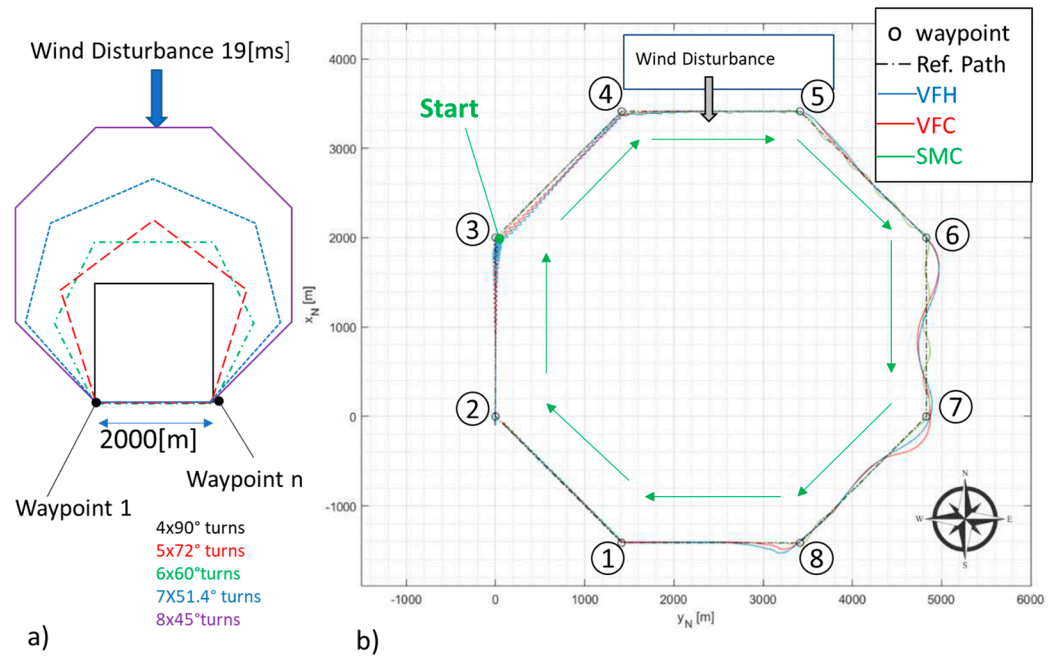
Figure 11. Different closed paths with polygonal shape (**a**), example of simulation performed with an octagonal one (**b**).
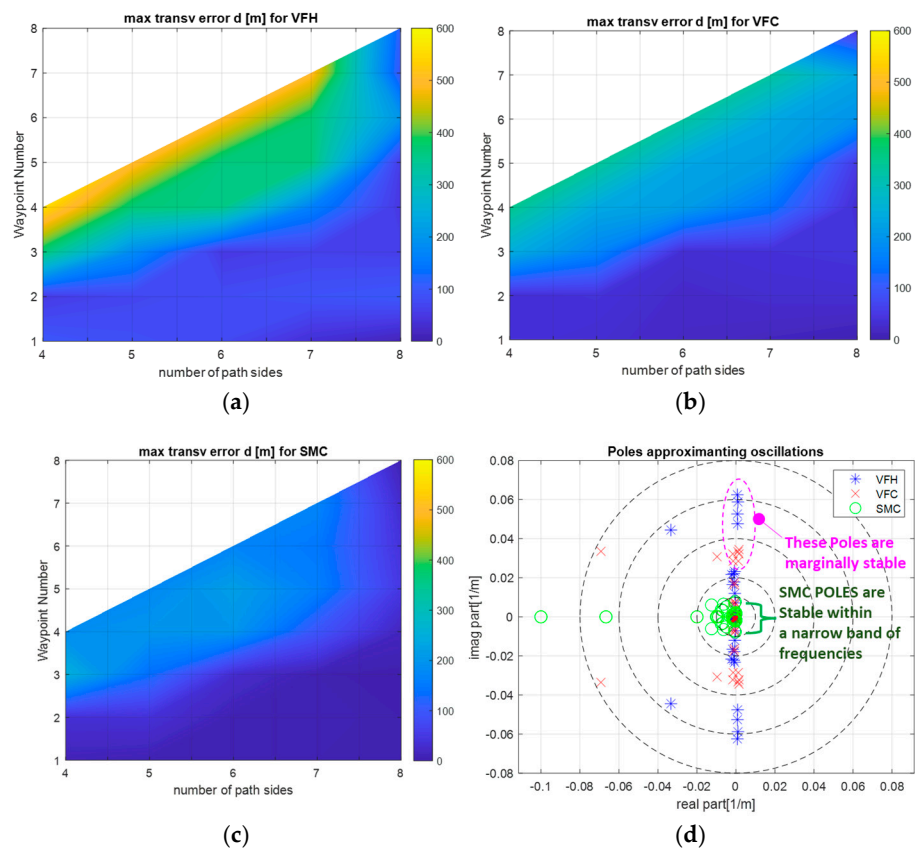
Figure 12. Max transversal error d measured after the turn on different waypoints with various path control algorithms (**a**–**c**), and corresponding poles approximating residual oscillations after each turn (**d**).

So, the behavior of $d(x_{traj})$ oscillations with respect to the traveled distances along the reference trajectory curve is approximated by the solution of the free response of the

homogeneous second order (28), assuming the transversal error $d(x_{traj\_i})$ and its derivative $d'(x_{traj\_i})$ at the i-th turn waypoint are known.

$$d''\left(x_{traj}\right) + 2\xi\omega_i d'\left(x_{traj}\right) + \omega_i^2 d(x_{traj}) = 0 \tag{28}$$

For a simpler implementation, (28) can be rewritten as the equivalent state space assuming a null input value u

$$\overbrace{\begin{bmatrix} d' \\ d'' \end{bmatrix}}^{\substack{\textit{State} \\ \textit{derivatives}}} = \overbrace{\begin{bmatrix} 0 & 1 \\ -\omega_i^2 & -2\xi_i\omega_i \end{bmatrix}}^{\substack{\textit{State} \\ \textit{Matrix A}}} \overbrace{\begin{bmatrix} d \\ d' \end{bmatrix}}^{\textit{State}} \tag{29}$$

Coefficients ω_i and ξ_i are identified by minimizing the squared error between the approximating, linear system and the damped oscillation of the transversal error that is measured after a turn. The fitting tool used is the so-called "Response Optimizer" of Matlab Simulink. Results are shown in Figure 12d: the system is not linear and strongly influenced by the direction of incoming wind disturbance. So, the approximating poles calculated for each turn are different. However, approximating poles of VFH and VFC path control are widely dispersed, and also some poles are unstable. So, it can be concluded that the behavior of both control systems is more variable and nonlinear. Unstable poles are associated with conditions in which disturbance is longitudinally aligned with the vehicle: if the plane is going against the wind (in Figure 11b from waypoint 2 to 3), high-frequency chattering is recorded; otherwise, if the plane is blown by a stern wind from behind (in Figure 11b from waypoint 6 to 7), low-frequency poorly damped oscillations occur. Otherwise, for SMC, all the approximating poles are stable; when oscillations occur, the range of recorded frequencies is quite narrow and corresponds to periods between 100 and 600 m. So, it can be concluded that SMC assures a more repeatable and stable behavior with respect to wind direction and turning amplitudes. The population of simulations can be further increased; however, the higher robustness of the proposed controller for the benchmark UAV is quite evident.

### 4.4. Waypoint Transitions: Different Approaches and Corresponding Results

As shown in Figures 10 and 11, the areas around waypoints appear to be the most critical in terms of cross-track error. Path-following performance is particularly affected since the trajectory is not directly planned, but the result of the transition between references of two adjacent traits. The transition technique used previously is the most commonly adopted in autopilot systems. This classical technique involves forcing the transition between one waypoint and the next when entering the predefined circle of radius r_{wp}. The new route reference ψ_w is provided causing the convergence to the next trait. In spite of its simplicity, the following disadvantages are identified:

- No real desired path is planned within the circle, so the trajectory is unpredictable;
- The radius r_{wp} of the circle must be chosen within a limited range: too large a radius will cause loss of flight accuracy while too small a radius will cause an incapacity to reach the waypoint and start the maneuver.

In order to eliminate these disadvantages, different transition techniques were studied in the literature [24–26]. In this section, an alternative waypoint transition method is investigated. The new technique no longer relies on the radius r_{wp}, but it is activated by crossing a predefined line; moreover, throughout the transition, a circular arc is imposed as the desired flight path. The application of the introduced method requires some geometric variables, which can be deduced from the only versions of the traits to be traveled [27]:

- The angle α between the two adjacent traits of the path;
- The center of the orbit C, which always lies on the bisector of the angle α;
- The distance l along the path between the destination waypoint and the line L of the beginning/ending of the transition.

Figure 13 illustrates the mentioned variables in a generic transition scenario.
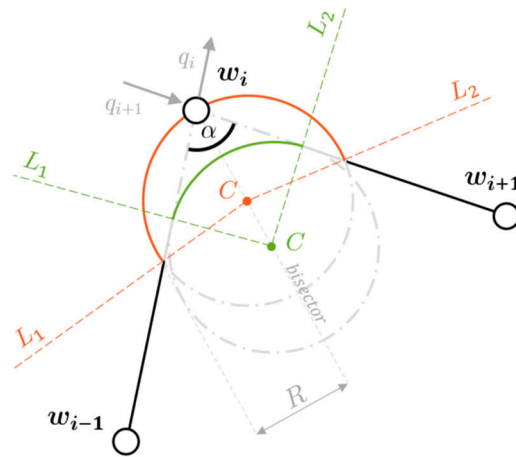
Figure 13. Orbit geometry and path planning in transition scenario.

The new technique involves the beginning and end of the transition at the crossing of lines L_1 and L_2, respectively, and causes the UAV to travel the arc of orbit between them. On the basis of the most common path-following requirements in aviation, a variation to the technique just presented is added, which differs in the imposed circle center. Both the geometries are shown in Figure 13. We fixed the orbit radius R rather than inscribing the transition circle at the angle α (green), and a circumscribed trajectory passing through the destination waypoint is defined (orange). These two techniques henceforth are identified as inscribed techniques and circumscribed techniques. Similarly to the classical technique, where the reference change occurs in advance of reaching the waypoint, in both the two new transitions, the orbit reference is also provided in advance with respect to the L_1 line crossing: this adjustment is intended to compensate for delays related to inertia and flight dynamics. In order to better appreciate their behavior, results are shown relative to the first turn of the square scenario with no wind implemented. Figure 14 plots both references and real trajectories for every technique and highlights the uncontrolled overshoot of the classical technique compared to the other two.

The results shown in Table 3 refer instead to the entire square path scenario, where for each technique, the benchmarks are calculated with respect to the corresponding reference paths. As confirmed by the table, the inscribed technique involves the best performance; indeed, its orbit arc is always tangent to the straight traits, thus facilitating remaining on the desired path. Before one transition is preferable, however, it should be considered that these two techniques meet different needs:

- The inscribed technique minimizes time and distance traveled by anticipating the turn and thus avoiding passing over the waypoint;
- The circumscribed technique instead imposes the reaching of the waypoint but increases the desired path length and thus the associated fuel consumption consequently.

Depending on mission requirements, it may be convenient to renounce better performance to ensure the proper waypoint achievement. Both the new techniques are significantly better performing than the original anyway because of a proper definition of the guidance problem and path around waypoints.
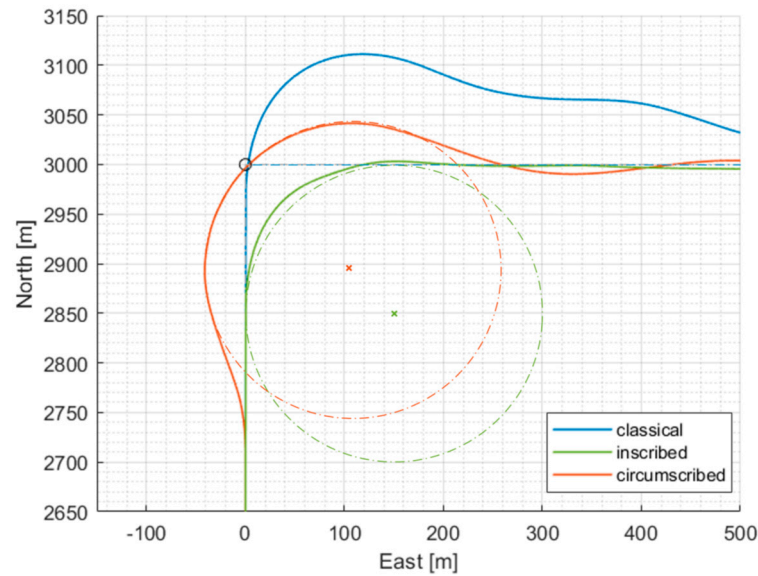
Figure 14. Comparison of transition techniques.

Table 3. Performance of transition techniques on the overall square route.

	$\|\|d\|\|_1$ [m]	RMSE(d) [m]	Fuel [g]	Mission Duration [s]
Classical	17.45	30.65	47.90	385.72
Inscribed	2.74	6.72	41.27	373.81
Circumscribed	4.78	11.36	43.45	383.97

5. Conclusions

In this paper, a fixed-wing path-following method based on a sliding mode approach to vector field theory was developed. Due to Lyapunov's theory, this new guidance law ensures not only the asymptotic stability of the sliding surface but also, on the same principles, the convergence of the UAV to straight paths and circular orbits and the tolerance to constant wind disturbances. The obtained guidance law exploits the banking dynamics and guarantees good helmsman behavior due to the definition of the specific vector field. Flight simulations were conducted in a high-wind scenario for all the algorithms. The results show how the wind robustness of both is comparable and in the range of 80% of the airspeed (≈ 35 kn). The SMC, however, proved to be significantly better in terms of performance and efficiency of path following leading to the lowest average cross-track error, attested around 2.5 times the wingspan. Moreover, in terms of portability, it is only 15% slower than the VFC algorithm to be run. Finally, three different transition techniques were investigated. In the critical areas around waypoints, the SMC algorithm was modified to improve effectiveness over transitions; however, the choice of a solution strongly depends on the requirements of the assigned mission.

All the obtained results are quite reliable with respect to a real application: despite the simplified model used for the synthesis of the regulator, all the results are obtained with a complete model of UAV [17], which also reproduces the behavior of propellers, motor and energy management systems. For this reason, the model is also able to give precious feedback concerning fuel consumption. In this way, it is possible to verify that more precise control of the trajectory against wind disturbance introduces a modest acceptable increase in consumed energy without penalizing too much the desired autonomy. Another important result is represented by the sensitivity of calculated fuel consumption with respect to the cornering policy adopted on waypoints: circumscribed and inscribed transition methods proposed in this work offer a clear advantage not only in terms of

precision of the path following but also in energy efficiency. A future improvement to which authors are currently working regards obstacle avoidance [28] and its integration with the proposed path-following strategy in order to correct the path without affecting efficiency and autonomy too much.

References

1. Sujit, P.B.; Saripalli, S.; Sousa, J.B. Unmanned aerial vehicle path following: A survey and analysis of algorithms for fixed-wing unmanned aerial vehicles. *IEEE Control. Syst. Mag.* **2014**, *34*, 42–59.
2. Conte, G.; Duranti, S.; Merz, T. Dynamic 3D path following for an autonomous helicopter. *IFAC Proc. Vol.* **2004**, *37*, 472–477. [CrossRef]
3. Ambrosino, G.; Ariola, M.; Ciniglio, U.; Corraro, F.; De Lellis, E.; Pironti, A. Path generation and tracking in 3-D for UAVs. *IEEE Trans. Control. Syst. Technol.* **2009**, *17*, 980–988. [CrossRef]
4. Wang, Y.; Wang, X.; Zhao, S.; Shen, L. Vector field based sliding mode control of curved path following for miniature unmanned aerial vehicles in winds. *J. Syst. Sci. Complex.* **2018**, *31*, 302–324. [CrossRef]
5. Ratnoo, A.; Sujit, P.B.; Kothari, M. Adaptive optimal path following for high wind flights. *IFAC Proc. Vol.* **2011**, *44*, 12985–12990. [CrossRef]
6. Dacic, D.B.; Nesic, D.; Kokotovic, P.V. Path-following for nonlinear systems with unstable zero dynamics. *IEEE Trans. Autom. Control* **2007**, *52*, 481–487. [CrossRef]
7. Ostertag, E. An Improved Path-Following Method for Mixed H2/H∞ Controller Design. *IEEE Trans. Autom. Control* **2008**, *53*, 1967–1971. [CrossRef]
8. Nelson, D.R.; Barber, D.B.; McLain, T.W.; Beard, R.W. Vector field path following for miniature air vehicles. *IEEE Trans. Robot.* **2007**, *23*, 519–529. [CrossRef]
9. Beard, R.W.; Ferrin, J.; Humpherys, J. Fixed wing UAV path following in wind with input constraints. *IEEE Trans. Control. Syst. Technol.* **2014**, *22*, 2103–2117. [CrossRef]
10. Shah, M.Z.; Samar, R.; Bhatti, A.I. Guidance of air vehicles: A sliding mode approach. *IEEE Trans. Control. Syst. Technol.* **2014**, *23*, 231–244. [CrossRef]
11. Ali, S.U.; Samar, R.; Shah, M.Z.; Bhatti, A.I.; Munawar, K.; Al-Sggaf, U.M. Lateral guidance and control of UAVs using second-order sliding modes. *Aerosp. Sci. Technol.* **2016**, *49*, 88–100. [CrossRef]
12. Chen, P.; Zhang, G.; Li, J.; Chang, Z.; Yan, Q. Path-Following Control of Small Fixed-Wing UAVs under Wind Disturbance. *Drones* **2023**, *7*, 253. [CrossRef]
13. Coelho, P.; Nunes, U. Path-following control of mobile robots in presence of uncertainties. *IEEE Trans. Robot.* **2005**, *21*, 252–261. [CrossRef]
14. Labbadi, M.; Cherkaoui, M. Robust integral terminal sliding mode control for quadrotor UAV with external disturbances. *Int. J. Aerosp. Eng.* **2019**, *2019*, 2016416. [CrossRef]
15. Nian, X.H.; Zhou, W.X.; Li, S.L.; Wu, H.Y. 2-D path following for fixed wing UAV using global fast terminal sliding mode control. *ISA Trans.* **2023**, *136*, 162–172. [CrossRef]
16. Aguiar, A.P.; Hespanha, J.P. Trajectory-tracking and path-following of underactuated autonomous vehicles with parametric modeling uncertainty. *IEEE Trans. Autom. Control* **2007**, *52*, 1362–1379. [CrossRef]
17. Casazza, A.; Fiorenzani, R.; Mela, A.; Pugi, L.; Reatti, A. Modelling of Unmanned Aerial Vehicles with Vertical Take off and Landing Capabilities. In *International Workshop IFToMM for Sustainable Development Goals*; Springer: Cham, Switzerland, 2021; pp. 255–263.
18. Beard, R.W.; McLain, T.W. *Small Unmanned Aircraft: Theory and Practice*; Princeton University Press: Princeton, MJ, USA, 2012.

19. Rysdyk, R. UAV path following for constant line of-sight. In Proceedings of the 2nd AIAA "Unmanned Unlimited" Conference and Workshop and Exhibit, San Diego, CA, USA, 15–18 September 2003; p. 6626.

20. Park, S.; Deyst, J.; How, J.P. Performance and lyapunov stability of a nonlinear path following guidance method. *J. Guid. Control. Dyn.* **2007**, *30*, 1718–1728. [CrossRef]

21. Machmudah, A.; Shanmugavel, M.; Parman, S.; Manan TS, A.; Dutykh, D.; Beddu, S.; Rajabi, A. Flight Trajectories Optimization of Fixed-Wing UAV by Bank-Turn Mechanism. *Drones* **2022**, *6*, 69. [CrossRef]

22. Kim, K.J.; Park, J.B.; Choi, Y.H. Chattering free sliding mode control. In Proceedings of the 2006 SICE-ICASE International Joint Conference, Busan, Republic of Korea, 18–21 October 2006; pp. 732–735.

23. Borup, K.T.; Fossen, T.I.; Johansen, T.A. A nonlinear model-based wind velocity observer for unmanned aerial vehicles. *IFAC-PapersOnLine* **2016**, *49*, 276–283. [CrossRef]

24. Beard, R.W.; Humpherys, J. Following straight line and orbital paths with input constraints. In Proceedings of the 2011 American Control Conference, San Francisco, CA, USA, 29 June–1 July 2011; pp. 1587–1592.

25. Capello, E.; Guglieri, G.; Quagliotti, F.B. UAVs and simulation: An experience on MAVs. *Aircr. Eng. Aerosp. Technol.* **2009**, *81*, 38–50. [CrossRef]

26. McLain, T.; Beard, R.W.; Owen, M. Implementing dubins airplane paths on fixed-wing uavs. In *Handbook of Unmanned Aerial Vehicles*; Springer: Berlin/Heidelberg, Germany, 2014; Chapter 68; pp. 1677–1701.

27. Kikutis, R.; Stankūnas, J.; Rudinskas, D. Autonomous unmanned aerial vehicle flight accuracy evaluation for three different path-tracking algorithms. *Transport* **2019**, *34*, 652–661. [CrossRef]

28. Bashir, N.; Boudjit, S.; Dauphin, G.; Zeadally, S. An obstacle avoidance approach for UAV path planning. *Simul. Model. Pract. Theory* **2023**, *129*, 102815. [CrossRef]